TRENDS IN SCIENCES 2025; 22(10): 10659
https://doi.org/10.48048/tis.2025.10659 RESEARCH ARTICLE

Multiscale Characterization and Optical and Radiation Absorption Behavior of Hybrid Nanocomposites for Advanced Applications

Sara J. Ahmed and Ehssan Al-Bermany*

Department of Physics, Faculty of Education for Pure Sciences, University of Babylon, Babylon, Iraq

(*Corresponding author's e-mail: ehssan@uobabylon.edu.iq)

Received: 15 May 2025, Revised: 12 June 2025, Accepted: 25 June 2025, Published: 30 July 2025

Abstract

Nanocomposites are advanced materials used experimentally in various applications, such as optical and industrial, and recently in radiation attenuation. This research aims to fabricate polycaprolactone/polyethyleneimine (PCL/PEI) blend polymer hybrid nanocomposites loaded with silicon dioxide (SiO_2) and graphene oxide (GO) nanomaterials to improve their performance and properties. The solvent casting method, assisted by sonication, was employed to create four samples: BP, NCP1, NCP2, and NCP3, which were cast in Petri dishes. Structural characterization was conducted using X-ray diffraction, Fourier transform infrared spectroscopy, optical microscopy, and field-emission scanning electron microscopy. The nanocomposites exhibited enhanced structural homogeneity and increased crystallinity due to the addition of both SiO_2@GO nanoparticles in NCP3 rather than a blend polymer or reinforcement with a single nanomaterial. The NCP3 sample exhibited notable enhancements in the most favourable results, including optical conductivity, dielectric constants, refractive index increase (36.5%), and extinction coefficient (42.1%) compared to the blend polymer. Furthermore, the real and imaginary dielectric constants showed improvements of 48.7% and 55.3%, respectively. The attenuation coefficients (μ) increased by 71.8% compared to the blend polymer, which was computed using a caesium-137 (662 keV) source. Furthermore, the measurements confirmed a significant improvement in radiation attenuation, indicating a synergistic effect between the nanofillers. Combined nanomaterials (SiO_2-GO) demonstrated superior performance compared to a single nanomaterial, rendering them an exceptional candidate for various advanced applications, particularly in light shielding or sanitary landfill of radioactive materials using lightweight concrete.

Keywords: SiO_2, GO, Optical properties, Radiation attenuation, Shielding

Introduction

The need to develop radiation-shielding materials that are lightweight, flexible, and highly efficient has arisen in recent years due to the increasing use of ionising radiation in medical, industrial, and nuclear applications [1]. While conventional materials, such as lead, are effective, they are burdened by environmental and health issues. Consequently, researchers have begun investigating safer and more sustainable materials [2]. Hybrid nanocomposites have garnered increasing attention among these alternatives due to their ability to integrate polymers with nanomaterials, enhancing their performance in radiation protection, particularly gamma rays [3]. Graphene and silica are among these materials that serve as effective mediators in nanocomposites [4]. This is a result of its distinctive characteristics, including a large surface area, lightweight nature, and capacity to interact with ionising radiation. Multiple studies have shown that incorporating nanomaterials into polymer matrices can induce structural changes at the nanoscale [5], improving radiation interaction behaviour through photon scattering and increased absorption potential [6].

Polyethyleneimine (PEI) and Polycaprolactone (PCL) were employed as the polymer matrix in this investigation due to their complementary chemical and physical properties. PCL is distinguished by its

exceptional flexibility and capacity to form films [7], whereas PEI is defined by its abundant amino groups, which serve as active sites for nanomaterial interaction [8]. Nanomaterials, including silicon dioxide and graphene oxide, were also employed. The increased surface area of these nanoparticles amplifies their interaction with incoming photons, thereby enhancing their radiation attenuation efficacy [9]. It is anticipated that integrating these materials into a cohesive polymer matrix will result in a synergistic effect, enhancing the absorption efficacy and the membranes' overall effectiveness in radiation shielding applications [10].

Kaew-On *et al.* [11] participated in the development of polymer composite sheets by mixing poly(vinylidene fluoride-co-hexafluoropropylene) or P(VDF-HFP) with different quantities of barium sulfate (BaSO4) for X-ray shielding purposes. The photon counting method was used to assess the composite shielding properties using the linear attenuation coefficient. Surface characteristics, encompassing surface morphology, hydrophobicity, and surface energy, were examined using an atomic force microscope (AFM) and a water contact angle apparatus. Scanning electron microscopy (SEM) was used to examine the microstructural distribution and dispersion of BaSO4 particles inside the polymer matrix, offering insights into the composite's homogeneity and structural integrity. The composite polymer sheets' bulk characteristics, including crystal structures, tensile strength, and thermal stability, were analysed. The findings indicate that raising the content of BaSO4 in BaSO4/P(VDF-HFP) composite sheets significantly enhances their X-ray attenuation properties. Furthermore, higher BaSO4 concentrations improve the material's hydrophobicity, flexibility, and thermal stability, underscoring the promise of these composites for sophisticated radiation shielding applications. In addition, in 2021, Paula *et al.* [12] examined the impact of PCL nanocomposite films including 0.5% MCM-48, whereby MCM-48-NH2 nanoparticles were transformed using (3-aminopropyl) triethoxysilane (APTES) and then exposed to gamma radiation at 25 kGy. The images obtained using MEV and TEM revealed the presence of nanoparticle aggregates randomly dispersed inside the films. This study aimed to investigate the impact of gamma radiation on nanocomposites. The solvent casting technique was used to produce the nanocomposite films. After processing the sample, it was subjected to gamma irradiation at a dose of 25 kGy in an aerobic atmosphere to study the effect of radiation on its structural and optical properties. Exposure to gamma radiation did not significantly alter the thermal or mechanical properties of NC films. The findings indicated that gamma radiation was an effective method for sterilizing these materials.

In a separate study, the integration of GO nanosheets, as shown by researchers [13]. Facilitates robust interfacial contact among components and modifies the XRD spectrum. The addition of GO demonstrated a substantial improvement in the optical, mechanical and thermal characteristics [14]. This enhancement markedly escalates with the rise of the GO ratio in the matrix. Nanocomposites were effectively accomplished with a homogeneous and fine dispersion of the GO nanosheets inside the matrix [15]. The optical characteristics exhibit enhancement owing to the substantial influence of GO nanosheets. The energy gap between the permitted and prohibited indirect transitions is enhanced by reducing the values [16]. The nanocomposites were first synthesized, and the findings demonstrated a significant capacity for radiation adsorption [17]. Consequently, it has shown potential for gamma-ray absorption and may serve as a radiation shielding material; moreover, it holds promise for several applications, including UV filters, solar cells, and specific optoelectronic uses [18].

Expanding upon this line of research, in 2022, Abdali [19] investigated SiO_2-based nanocomposites for gamma shielding, as well as polymer blends and composites (PB and PCs), which are novel materials with proven radiation protection capabilities. This study investigates the impact of adding silicon dioxide (SiO_2) nanoparticles (NPs) on the radiation shielding capabilities of carboxymethyl cellulose, poly(N-vinyl pyrrolidone), and polyethylene glycol. Depending on HVCMC/PVP/PEG with SiO_2 NPs, samples were designated k0, k1, k2, and k3. XRD, FTIR, and OM were used to characterize the structure. Additionally, the attenuation coefficients were calculated using Cs^{-137} sources. Results showed that increasing SiO_2 NPs from 0 to 0.045% increases the attenuation coefficient and decreases the (N/No) values, with 0.045% being the optimal doping level. The primary influence on GRS

characteristics occurred within the k3 samples for Cs^{137} radiation sources. To accomplish this, a variety of morphological, structural, and chemical functional analyses were performed, along with UV optical assessment, to elucidate the internal structure of the nanocomposites and their efficacy in absorbing or blocking light. In previous studies, the effects of both silicon dioxide SiO_2 and graphene oxide GO were investigated individually in nanocomposites; however, the 2 nanomaterials were not combined within a bi-polymer matrix.

The present study aims to investigate the synergistic effects of combining two polymers (PCL and PEI) with 2 nanomaterials (SiO_2 and GO) on the efficacy of radiation-shielding nanocomposite films. The reason for the nano synergy and enhancement is due to the ability of silicon dioxide to disperse, the high density of electrons, and the interfacial interaction of graphene oxide, which enables them to work together to improve the attenuation of gamma rays. Four unique samples were prepared: The basis polymer blend (BP), PCL-PEI/SiO_2 (NCP1), PCL-PEI/GO (NCP2), and PCL-PEI/SiO_2@GO (NCP3). The goals include assessing the impact of each composition on structural features (via XRD and FTIR), optical qualities (by UV-Vis spectroscopy), and gamma radiation attenuation efficacy utilizing Cs-137.

Materials and methods

PCL is a white powder with a MW of 80,000 $g•mol^{-1}$, and $(C_6H_{10}O_2)_n$ is the chemical Formula. PEI has an Mw of 25,000 $g•mol^{-1}$, and a chemical formula of $(C_2H_5N)_n$ and is light yellow. All ingredients necessary to create graphene oxide (GO) are described in the earlier paper [20]. The manufacturer of this material is Aldrich Chemistry, part of the Sigma-Aldrich group in the United Kingdom. High-purity (99.8%) white material is silicon dioxide. It is found in nanopowders, which are 20 - 30 nanometers. The source of this material was from Hongwu International Group Ltd., a Chinese company. The synthesis of graphene oxide was carried out, and all requirements were provided by Sigma-Aldrich, a UK company, with a purity of 99%. The synthesis methods and full characterization of the synthesized GO were reported in a previous publication [20].

Using chloroform, the PCL and PEI polymers were dissolved separately to create dissolved polymer samples. Both polymers were combined in equal proportions at 22 °C, with a 50:50 ratio. Chloroform was used to prepare the 2 nanomaterials, SiO_2 and GO, individually at a concentration of 0.2 g/50 mL. From these stock solutions, 25 mL of each aliquot containing 0.1 g of each nanomaterial was withdrawn. Each nanomaterial was placed on a stirrer for varying durations. At a rate of 5 h per day, SiO_2 was stirred for 5 days, while GO was stirred for 8 days under identical conditions. In addition, both materials were subjected to ultrasonic treatment for 5 min at half-hour intervals. The new (PCL-PEI/SiO_2) nanocomposites were developed by adding SiO_2 to the blended (PCL-PEI) at a weight percentage of 1%. After being agitated for 10 min per hour using sonication for the 1st 3 h, this mixture was continuously combined for 48 h, with 30 min of sonication in a sonication bath performed at 150W power and 40 Hz. The synthesized (PCL-PEI/GO) nanocomposite was subjected to the exact method. The (SiO_2@GO) nanoparticles are subsequently combined in a weight-per-cent loading ratio of (50:50) to create the fourth (PCL/PEI/SiO_2@GO) nanocomposite. The finished nanocomposites were molded onto Petri dishes and stored in a fume cabinet for three days to ensure complete drying and solvent removal. To prevent moisture absorption, store the desiccator with the dry nanocomposite samples. The digital micrometer was used to measure the 80 ± 10 μm thickness of the nanocomposite samples. **Table 1** presents the ratio of sample preparation.

Table 1 Weight percentage of the prepared samples.

Samples	Weight percentage %			
	PEI	PCL	SiO_2	GO
BP	50	50	0	0
NCP1	49.5	49.5	1	0

Samples	Weight percentage %			
	PEI	PCL	SiO_2	GO
NCP2	49.5	49.5	0	1
NCP3	49	49	1	1

This investigation's instruments and technical specifications are as follows: FTIR measurements were performed with a Perkin Elmer Spectrum IR-10.62, covering a range of 500 - 4000 cm^{-1} in the USA. XRD analysis was conducted using a PANalytical AERIS, ranging from 5° to 80° (Netherlands). The FESEM analysis employed the INSPEC F50 manufactured by FEI (Netherlands). A Shimadzu UV-2100 was utilized for UV-Vis spectroscopy, functioning throughout the 190 - 110 nm region (Japan). Optical microscopy (OM) was performed using a Nikon 73364 microscope from Olympus, providing magnification of up to 40× (Japan). Double beam spectrophotometer type Shimadzu, UV-1800, with wavelength range (200 - 1100), utilized to characterize the samples at room temperature. The average thickness of the prepared films reached 80 micrometres. Use a blank reference film (polymer matrix without nanomaterials) to ensure data accuracy. The Giger probe and device connected to the software were used to obtain absorption data from the computer.

Gamma-ray attenuation measurement setup

Gamma-ray attenuation experiments of blended polymers and nanocomposites were conducted to examine the attenuation characteristics of gamma rays in samples with varying concentrations of GO and SiO_2 nanoparticles. Test samples with varying concentrations were positioned in front of a collimated beam emanating from a caesium-137 (Cs137, with 662 keV) gamma-ray source. The gamma-ray source is located 3 cm from the detector, whereas the nanocomposite samples are situated 5 cm from the gamma-ray source. detector type (NaI (Tl)), and counting time (300 s). The gamma-ray fluxes transmitted through the samples are quantified using a Geiger counter, which was used to calculate the linear attenuation coefficients. The Geiger counter comprises a Geiger-Müller tube, which detects radiation, and the electronics that process and present the results. The Geiger-Müller tube contains a gas, such as helium, neon, or argon, at minimal pressure, subjected to high voltage. The electrical charge will be conducted down the tube when an incoming particle or photon ionizes the gas, making it conductive [21].

The attenuation coefficient μ is approximately proportional to the material density, where (μ_m) is frequently used instead of (μ). The mass attenuation coefficient is obtained by dividing μ by the material density (ρ) [22].

$$\mu_m = \frac{\mu}{\rho} \quad (1)$$

The value of (μ_m) is approximately constant for all materials. The absorption The law for gamma particles can be written in the appropriate form depending on Equation order [22].

$$N = N_o\, e^{-\mu x} \quad (2)$$

where N is the number of photons passing through the thickness x of the absorber [23]. For radiation protection design, a commonly specified entity is the half-value thickness, which characterizes suitable materials for any particular type of radiation and the energy involved. As the name indicates, this number directly gives the thickness required to reduce the intensity of the incoming radiation by half. For calculations, the more fundamental attenuation coefficient) μ) is preferred, which, of course, is related to the half-value thickness Eq. (3) [24].

$$x^{1/2} = \frac{\ln 2}{\mu} \quad (3)$$

$x^{1/2}$ and (μ) depends on the material of the absorber and the energy of the radiation [25].

Results and discussion

The FTIR in **Figure 1** of the sample reveals structural changes resulting from incorporating GO and SiO_2 into the PCL-PEI matrix. Distinct peaks around 2922 cm^{-1} correspond to symmetric C-H stretching vibrations [26], while the peaks observed in the range

between 1558 - 1583 cm^{-1} are attributed to N-H bending vibrations from PEI [27]. Peaks at around 1106 - 1070 cm^{-1} are associated with C-O-C and Si-O-Si stretching vibrations, confirming the integration of silica within the polymer structure [28]. The spectrum alterations signify robust intermolecular interactions between the polymer matrix and the nanofillers, suggesting improved structural uniformity. These interactions may enhance the nanoparticle's structural stability and dispersion within the polymer [29].

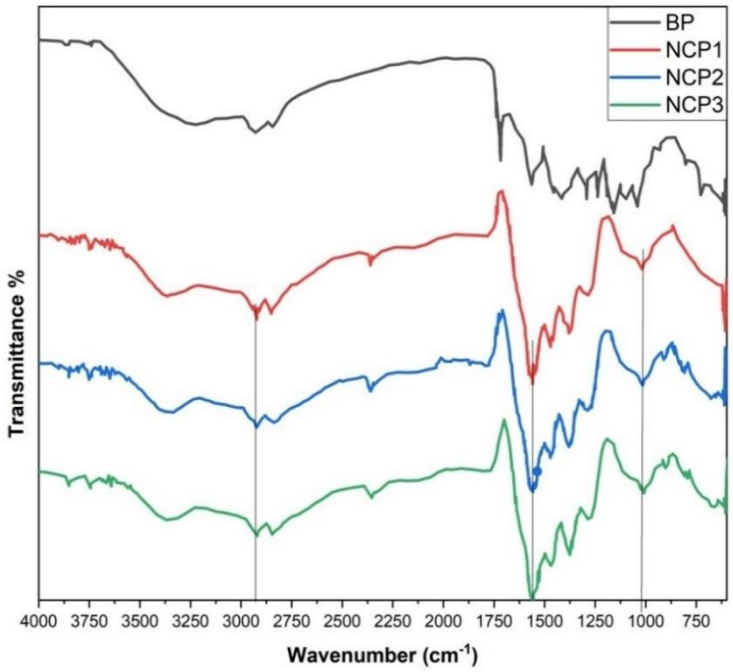

Figure 1 FTIR spectra examination of nanocomposites.

XRD examination in **Figure 2** indicated that the integration of PEI and PCL polymers resulted in structural alteration without the emergence of a new phase, and the addition of (SiO_2@GO) nanomaterials enhanced crystallinity owing to the interaction between nanoparticles and polymer chains [30]. The pronounced XRD peaks at 21 and 23, which rise to 118 and 34 cps, respectively, demonstrate a more significant structural order than the 1st mix compared with JCPDS Card Nos. 0-1431 for PCL, JCPDS card 72-2303 for PEI, JCPDS card No. 00-041-1487 for GO and JCPDS card 29-0085 of SiO_2. Whereas introducing (SiO_2@GO), nanomaterials revealed a slight shift to the higher value of the peaks to ($2\theta = 21.62°$) and ($2\theta = 23.92°$) compared with all samples. The increase in crystallinity observed in the NCP3 nanocomposite can be assigned to the influence of the SiO_2 and GO nanoparticles, which act as nucleating agents that enhance the alignment and ordering of polymer chains [31].

Eq. (4) was derived from Bragg's principles. The interplanar d-spacing was obtained by examining the peak position [32].

$$n\lambda = 2dsin(\Theta) \quad (4)$$

The variables (n), (λ), (d), and (Θ) in this equation are the integers representing the entering X-ray wavelength, d-spacing, and the angle among the radiation and the scattering plane. The crystallite size (D) in nanometers was determined by applying the Scherrer formula [33].

$$D = k\lambda / \beta cos(\Theta) \quad (5)$$

$$\varepsilon = \beta / 4\tan(\theta) \quad (6)$$

The variables (k) and (β) represent the form factor and the total width at half-maximum (FWHM) of the crystal mean, respectively. The current value of (k) is

roughly 0.9. **Table 3** shows the inclusion of the crystallinity of the nanocomposites.

The Scherrer equation indicates that an increase in crystallite size (D) is associated with a rise in peak intensity in the XRD pattern. This results from fewer microstructural distortions and grain boundary influences, facilitating more effective X-ray diffraction. The noted increase in peak intensity confirms the enlargement of crystallite size and the improvement in crystallinity.

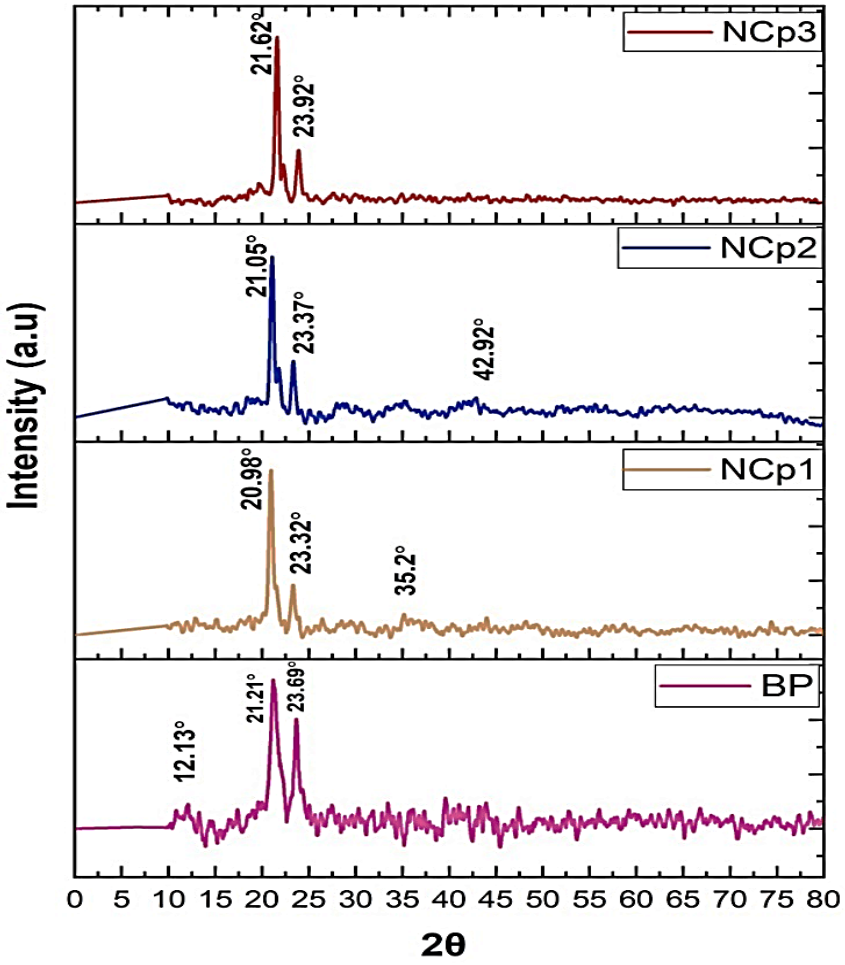

Figure 2 The XRD patterns for the sample.

Table 2 shows the samples' peak positions, FWHM, d, crystallite size, and Lattice strain.

Specimens	Peak position 2θ (°)	FWHM (β)	d (nm)	D (nm)	Average D (nm)	(Ɛ) %	Average (Ɛ) %×10^{-3}
BP	12.13	2.2042	0.729	35.72078849	29.02	0.0095	8
	17.23	2.368	0.729	26.63952381		0.010	
	21.21	0.3149	0.418	26.79666129		0.0073	
	23.69	0.3149	0.375	26.91200682		0.0065	
NCP1	20.98	0.1574	0.424	35.71175136	29.66	0.0037	3.1
	23.32	0.2755	0.382	26.89393472		0.0058	
	35.2	0.2362	0.205	27.63241002		0.0019	
	43.96	0.4723	0.206	28.40347438		0.0009	
NCP2	9.83	0.1181	0.899	35.24448761		0.0005	
	21.05	0.2362	0.421	26.80945055		0.0055	

Specimens	Peak position 2θ (°)	FWHM (β)	d (nm)	D (nm)	Average D (nm)	(Ɛ) %	Average (Ɛ) %×10^{-3}
	23.37	0.1574	0.379	26.89635909	29.31	0.0033	2.6
	42.92	0.3149	0.210	28.3009709		0.0012	
	10	0.0787	0.883	35.24902328		0.0003	
	18.6	0.2362	0.476	26.68977331		0.0001	
NCP3	21.62	0.2362	0.410	26.81479648		0.0010	
	23.92	0.2362	0.371	26.92339462	24.94	0.0010	1.3
	27.6	0.9446	0.322	9.041572751		0.0040	

Crystallisation denotes the qualitative enhancement in diffraction results, whereby the crystal size D is quantitatively determined using the Scherrer equation, excluding the calculation of the overall crystallinity index. The increasing value of the lattice strain (Ɛ) reveals the existence of distortions inside the lattice owing to the presence of nanomaterials. These distortions subsequently result in alterations in interatomic distances, hence influencing physical qualities such as hardness and structural stability. Those with high strain may display a more disordered structure, whereas those with low strain exhibit a more crystalline and regular structure [34].

Figure 3 shows the OM images of the surface of BP (NCP1), (NCP2), and quaternary (NCP3) nanocomposites, with magnification (40×). The image of the surface morphology of the pure blend polymer (PCL-PEI) revealed a comparatively even and consistent texture, suggesting a homogeneous combination of the two polymers. The absence of noticeable aggregation or phase separation indicated a high level of compatibility between PCL and PEI. The surface of the (PCL-PEI-SiO_2) turned less smooth and more uneven when SiO_2 was added to the mixed polymer. It may attribute the observed roughness to SiO_2-distributed nanoparticles throughout the polymer matrix [35].

Furthermore, when adding graphene oxide to a polymer blend (PCL-PEI/GO), the image revealed rough morphology and presented good dispersion of graphene-oxide nanosheets and aggregation of some nanosheets also presented [36], which was related to attraction by van der Waals forces as reported by several investigations [37]. Regarding the image of the addition of SiO_2 and GO nanomaterials to the polymer mix, it increased the roughness. This rise may be due to GO nanosheets, which are known to form a more varied and diverse surface structure. The uniformity of the distribution of GO nanosheets and SiO_2 nanoparticles improves the characterization of the nanocomposite. Demonstrates excellent dispersion of nanoparticles throughout the polymer matrix, resulting in improved structural and functional characteristics. The challenges in this procedure stem from the combined impacts of SiO_2 nanoparticles and GO nanosheets, as seen in **Figure 3**. The surface morphology displays increased intricacy, typified by a rough and diverse form.

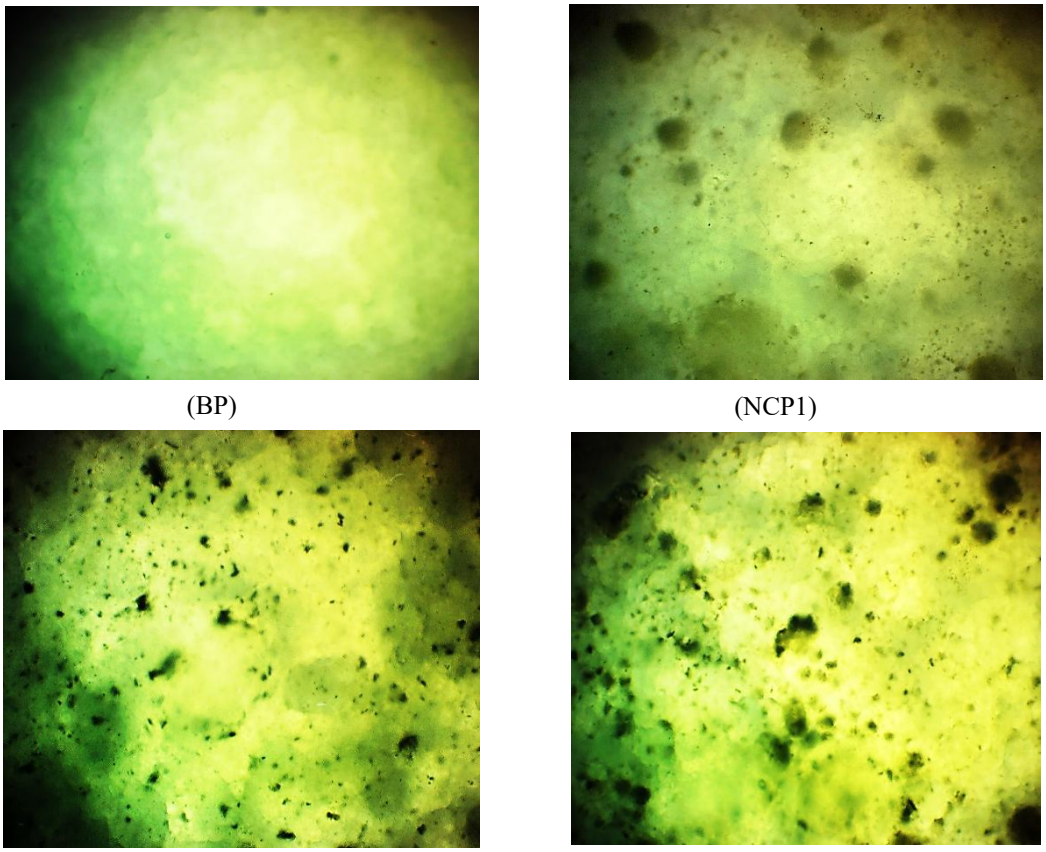

Figure 3 OM photomicrographs (40×) for blend polymers and samples.

Figure 4 presents FESEM images of BP, NCP_1, NCP_2, and NCP_3. A homogeneous BP surface exhibited fissures and grains. Literature indicates [38] that PCL and PEI's chemical and physical compatibilities may reveal areas where the constituent materials have aggregated or coalesced, exhibiting both soft and hard segments on the surface. SiO_2 improved sample homogeneity in the polymer mix. SiO_2 particles enhance interfacial cohesion by increasing dispersion and decreasing aggregation. (NCP_2) shows how GO affects GO surfaces. Its graphene oxide is evenly distributed, as seen by the tiny dots on the surface. Tiny dots suggest graphene oxide uniformity. Dispersion improves polymer matrix fracture resistance. In contrast to the other samples, (SiO_2@GO) nanoparticles are evenly dispersed throughout the (NCP_3) polymer matrix.

The surface roughness of the last sample (NP3) is attributed to the synergistic dispersion effect of the used nanomaterials (SiO_2@GO), as this is related to the optical conductivity and dielectric coefficients. Also, the surface inhomogeneity enhanced the attenuation of gamma rays due to the presence of many scattering centres [39]. The homogeneity and good dispersion of nanomaterials assist the films in resisting fracture because this homogeneity prevents stress concentration and contributes to easier load transfer within the matrix, which in turn hinders crack growth and improves strength properties [40].

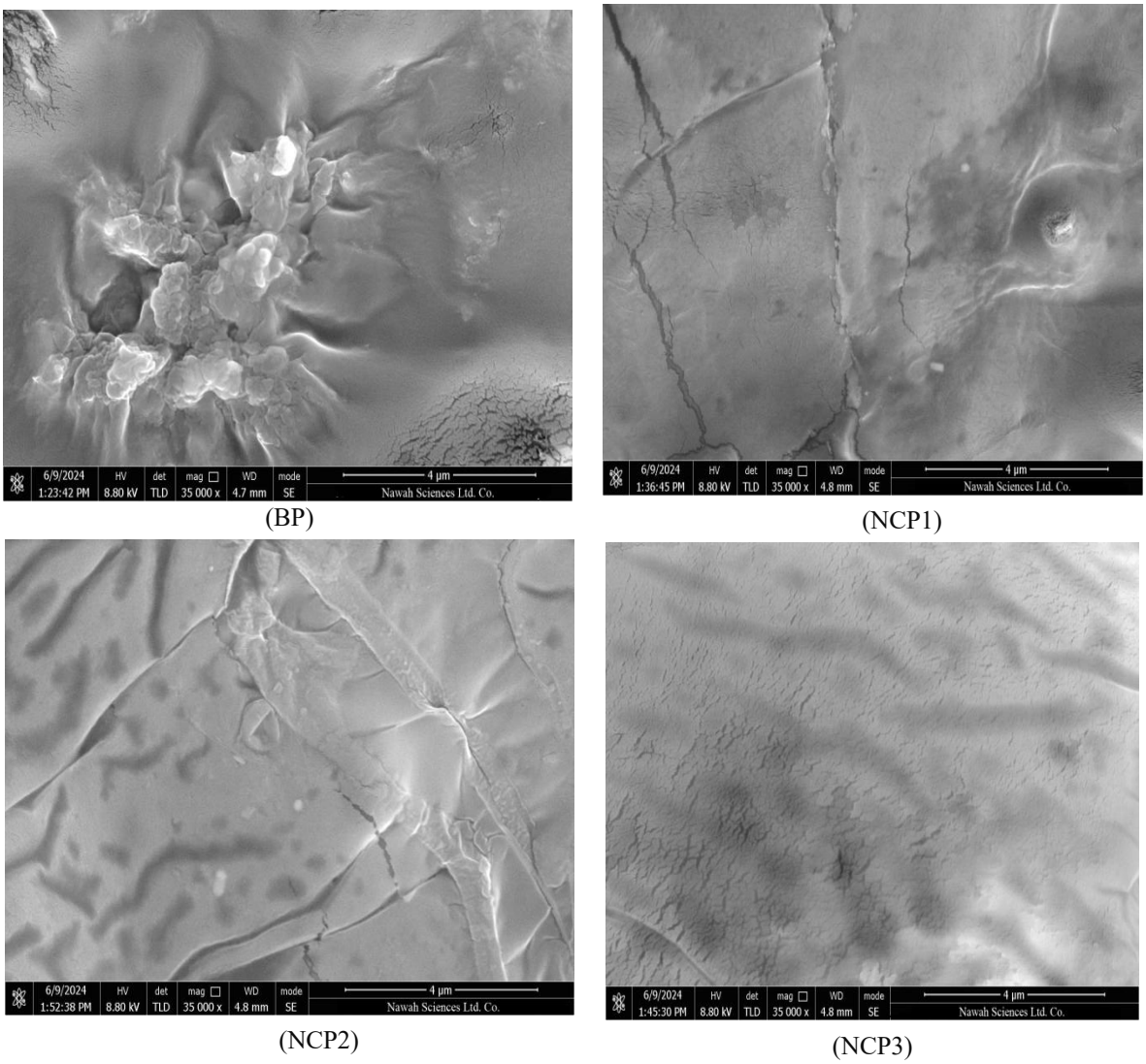

(BP) (NCP1)

(NCP2) (NCP3)

Figure 4 FESEM images and their nanocomposites.

The transmittance **Figure 5** indicates that the integration of nanomaterials into the polymer matrix (BP) led to a progressive reduction in light transmittance across the wavelength spectrum of 200 to 800 nm, signifying an enhancement in absorbance or light scattering within the synthesized nanocomposites NCP1, NCP2, and NCP3. The NCP3 sample had the lowest transmittance relative to the other samples, indicating that it has the maximum light absorption among all samples analyzed. The optical properties of these NCP3 nanocomposites provide them with a viable option for radiation shielding applications, including gamma-ray protection [41].

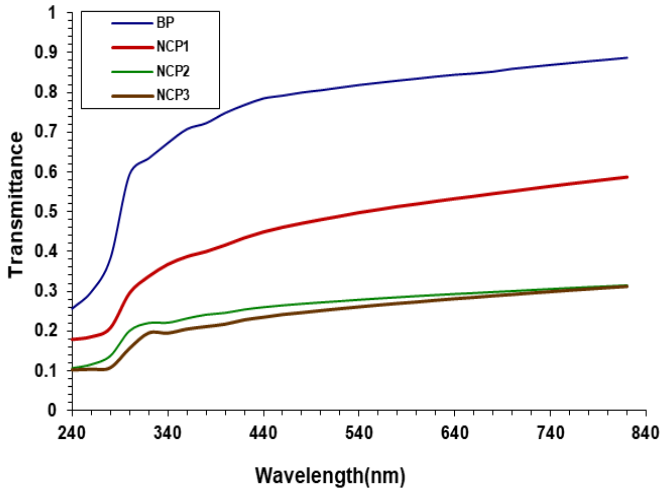

Figure 5 Spectral transmittance curves of nanocomposite samples in the 200 - 800 nm wavelength range.

The optical characteristics of the polymers and nanocomposites samples in **Figure 6** were examined using the refractive index (n) and the extinction coefficient (k), which together indicate the complex optical constants of the material. The results suggest that the 1st sample, which is composed of the blend polymer (PEI-PCL), has the lowest values in refractive index (n) and extinction coefficient (k)due to its high transmittance to radiation, and the highest value was in the last sample, NCP3, due to the addition of (SiO_2@GO) nanomaterials. This behaviour is due to the high levels of optical density and absorption of the material [42].

The ratio between the light speed in a vacuum and inside the substance is known as a refractive index (n), that given in Formula (7) [43].

$$n = \frac{1+\sqrt{R}}{1-\sqrt{R}} \quad (7)$$

(R) means the material reflectance.

The imaginary component of the complex refractive index (N) is known as the extinction coefficient, which is considered by Eq. (8) [44].

$$K_\circ = {}^{\alpha\lambda}/_{4\pi} \quad (8)$$

(λ) is the incident ray wavelength.

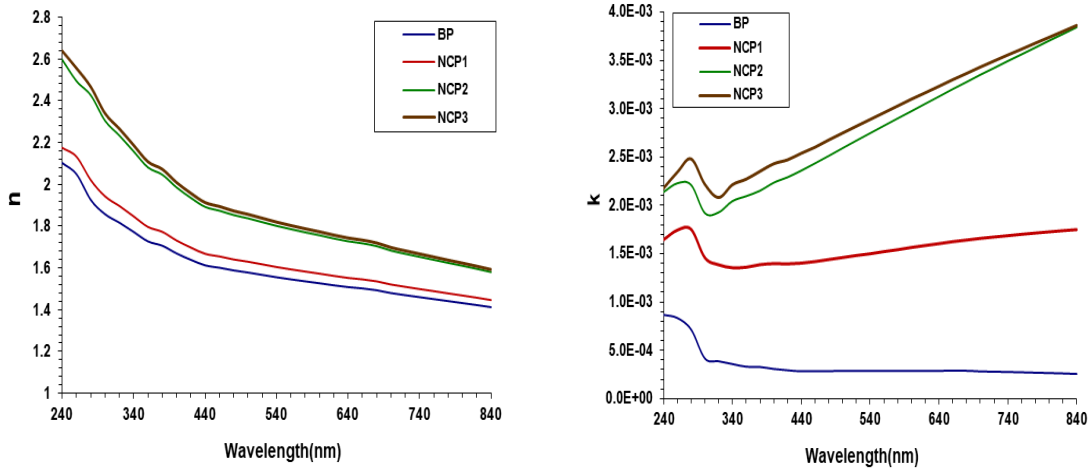

A B

Figure 6 (A) refractive index (n) and (B) extinction coefficient (K) as a function of the wavelength for samples.

The dielectric constant determines matter's capacity to polarize; it may respond to numerous frequencies very difficult, and electronic polarity dominates other forms of polarization. The real (ε_r) and imaginary (ε_i) dielectric constants may be calculated from Eq. (6) [45].

$$\varepsilon_r = \left(n^2 - K_\circ^2\right) \quad (6)$$

$$\varepsilon_i = (2nK_\circ) \quad (7)$$

According to Eq. (8), optical conductivity directly depends on the refractive index, absorption coefficient, and the light velocity in vacuum (c) [46].

$$\sigma_{op} = {}^{\alpha nc}/_{4\pi} \quad (8)$$

In **Figure 7**, the actual dielectric constant (ε_1) is plotted as a function of wavelength. ε_1 is a measure of the material's capacity to store photoelectric energy without incurring losses. In samples BP, NCP1, NCP2, and NCP3, the optical constant increases as the wavelength increases, signifying a diminished optical insulation response [47]. At the wavelength range of 240 - 280 nm, a notable rise in ε_1 is observed progressively from BP, NCP1, and NCP2 with the addition of the nanomaterial, reaching its peak in sample NCP3. This suggests that the integration of nanomaterials (SiO_2@GO) into the polymer matrix augmented the polarization property and elevated the density of electrons interacting with the optical field, hence enhancing electrical energy [48]. While the imaginary dielectric constant (ε_2) reflects the energy loss within the material due to light absorption, it expresses optical losses [49]. The BP sample shows the lowest energy absorption.

In contrast, the NCP3 sample shows the highest value, which indicates that it absorbs the most significant amount of photoelectric energy due to the enhancement of electronic transitions in the presence of nanoparticles [50]. This reflects an improvement in the optical properties of the system, both in its ability to store energy and in its absorption of electromagnetic radiation [5]. The effect of nanomaterials has led to an improvement in the optical properties, making the NP3 model more suitable, which could make it one of the promising applications in radiation protection [51].

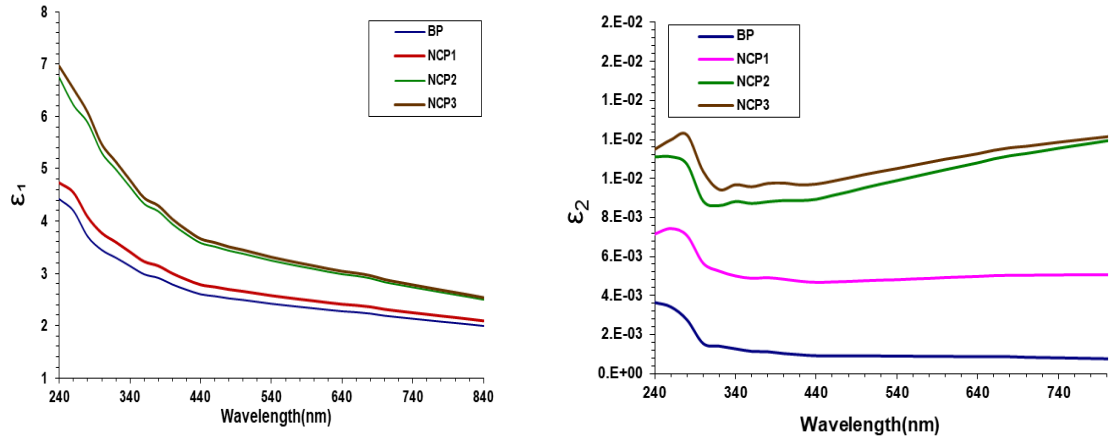

A B

Figure 7 Curves representing the actual component ε_1 and imaginary part ε_2 of the dielectric constant of materials (BP, NCP1, NCP2, and NCP3) in the ultraviolet range.

Figure 8 illustrates the correlation between optical conductivity, measured in $(S)^{-1}$, and wavelength (nm) for 4 samples. The results demonstrate that the optical conductivity in NCP1, NCP2 and NCP3 exhibits superior values relative to BP. At wavelengths 240 - 340 nm, whereas sample NCP3 exhibited the best results of conductivity, followed by NCP2 and NCP1 [52]. This phenomenon is ascribed to the elevated density of free electronic states and the augmented responsiveness of the material to electromagnetic radiation resulting from the presence of SiO_2@GO nanomaterial. The spectrum indicates that conductivity diminishes progressively

with rising wavelengths, a typical phenomenon attributed to less photon absorption at elevated wavelengths [53]. In comparison to the literature [54], the NCP3 sample exhibited a significant increase in conductivity, surpassing the optical conductivity of traditional composites made from SiO_2-supported PMMA materials. Furthermore, the absorption spectra demonstrated a wider and more pronounced absorption in the ultraviolet and visible regions, which is advantageous for radiation mitigation via the photon absorption mechanism. This enhancement results from the synergistic impact of SiO_2@GO nanoparticles in our present study.

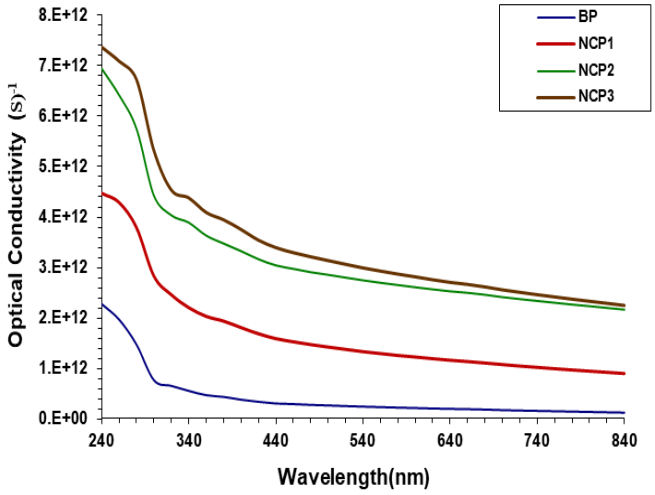

Figure 8 Spectral of optical conductivity in nanocomposites.

The absorption coefficient of lead of the gamma radiation from a given source [23]. The absorption law for gamma particles can be written in the appropriate form, depending on Eq. (2) [22]. In **Figure 9**, the efficacy of the nanocomposite samples in radiation attenuating gamma-rays N and radiation attenuation (N), which represents the number of photons that passed through the sample, and radiation particle number (No). Ln (N) and the ratio (N/No) are the fundamental metrics for evaluating the efficiency of gamma radiation attenuation. The results show a significant decrease in the (N/No) ratio, gradually when adding nanomaterials in an ascending manner, when adding nanomaterials to samples NCP1, NCP2, and NCP3, and thus an increase in the absorbance of gamma rays. This is attributed to the increased interaction between photons and nanomaterials, which are characterized by their high surface area. The sample showed the lowest transmittance ratio and, thus, the highest absorbance due to the scattering and absorption of photons, which is consistent with the literature [55].

Table 3 The percentage of improvement in optical metrics, attenuation coefficient, and conductivity between the BP and NP3 samples.

Property	Blend polymer	NP3	Improvement %
Optical conductivity σ_{op}	2.2×10^{12} S^{-1}	7.3×10^{12} S^{-1}	231.8%
Attenuation coefficient (μ)	3.6 cm^{-1}	5.45 cm^{-1}	51.4%
Real dielectric constant ε_1	4.4	6.5	47.7%

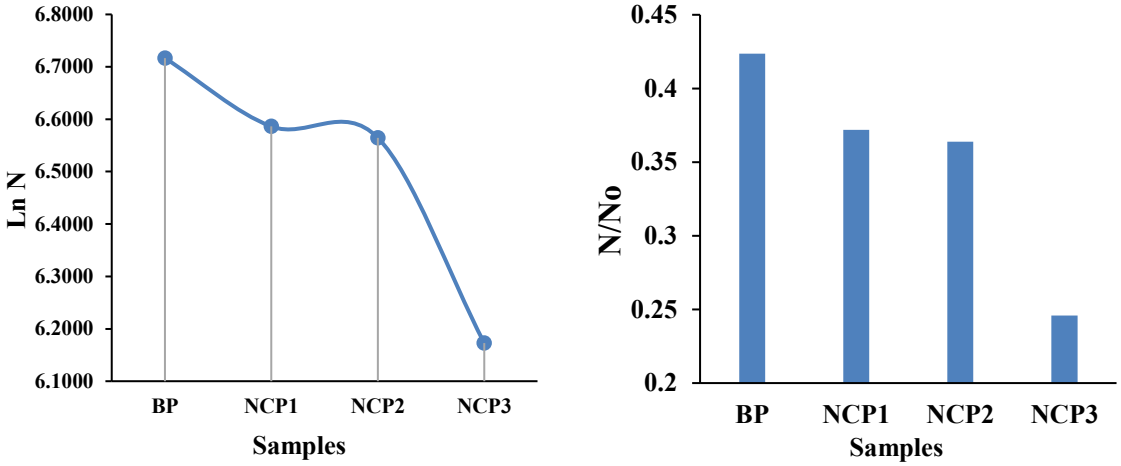

(A) (B)

Figure 9 Gamma-Ray attenuation assessment of Nanocomposite sample thickness based on (A**)** (Ln N) and (B) (N/No), where N represents the number of gamma-ray counts per second (count/s).

Figure 10 illustrates the variation in the absorption coefficient for the nanocomposite samples BP, NCP1, NCP2, and NCP3. The findings indicate a considerable enhancement in the value of (μ), which is the radiation attenuation factor, by incorporating nanomaterials. The samples enhance their gamma-ray absorption with the augmentation of nanomaterials. The minimum absorption value was observed at BP, whereas the maximum absorption value was noted at NCP3, attributed to incorporating SiO_2@GO nanoparticles. This demonstrates their superior efficacy in radiation shielding [56].

The other **Figure 10(B)** illustrates the extent of radiation inhibition for each sample by decreasing the photon count relative to the No condition, whereby no material is employed. Incorporating nanoparticles into the polymer matrix (from NCP1 to NCP3) resulted in a progressive reduction in the quantity of penetrating photons-matter interaction mechanisms, depending on the gamma-ray energy and the material's atomic number. Sample NCP3 had the most significant inhibition rate, hence validating the efficacy of nanoparticles in radiation protection [57].

Another important parameter in the shielding radiation is the half-value layer (HVL). It gives the information about shielding properties of a given absorber. It can be calculated from the Eq. (9).

$$HVL = {}^{\ln(2)}/_{\mu} \approx {}^{0.693}/_{\mu} \quad (9)$$

where, the HVL value represented the thickness for the shield. It reduces the incident radiation beam intensity by 50%. This means the lower HVL value evidences of more effective shielding properties of the applied shield. **Table 4** showed a brief comparative of Half value layer (HVL), attenuation coefficients for paraffin-based composites from this investigation compared to HVL values of other composites (from literature data), which contained lead (or lead compounds) and bismuth (or bismuth compounds) in their composition with NCP3 compare. These results reveled an interesting nanocomposite with lower filling ratio compared with metals like PbO with higher ratio.

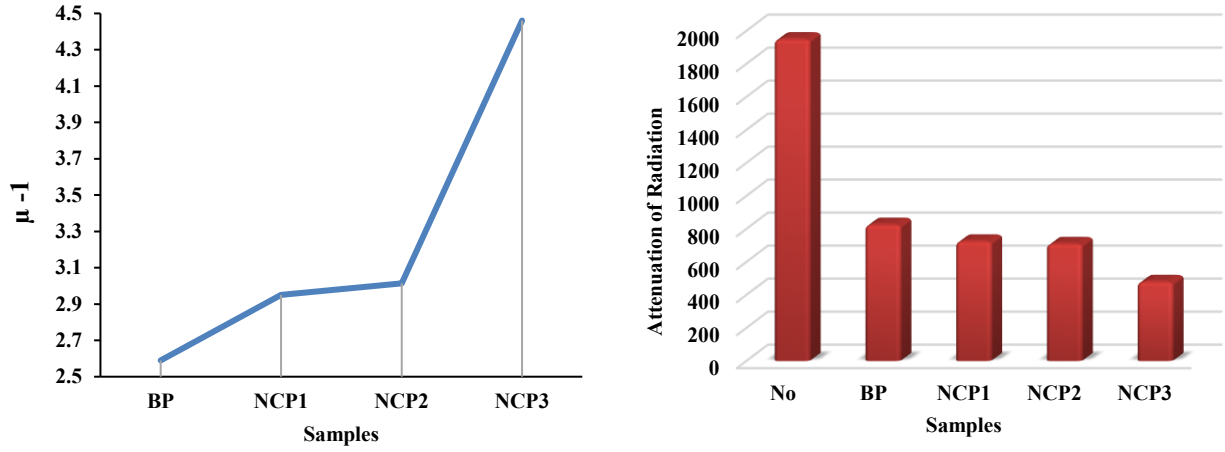

(A) (B)

Figure 10 (A) Linear attenuation coefficient (μ) of fabricated nanocomposite, and (B**)** radiation attenuation relative to the sample condition.

Table 4 A brief comparative of Half value layer (HVL), attenuation coefficients for paraffin-based composites from this investigation compared to HVL values of other composites (from literature data), which contained lead (or lead compounds) and bismuth (or bismuth compounds) in their composition, with NCP3 compared.

Material	Approx. HVL	Attenuation (Relative)	Filler Type	Pros	Percentage %	Cons	Ref.
Ceramic-Pbo	~3.5 cm	low	PbO	Excellent shielding	10%	Toxicity, heavy	[58]
PMMA-Bi	~3.65 cm	low	Bi	Non-toxic alternative	60%	Non-Toxicity	[59]
OUP, MEKP, Co-6, Bi	~3.89 cm	low	Bi	Durable and effective	50%	Non-Toxicity	[60]
PCL-PEI/ SiO_2@GO	Likely > 3.5 cm	Low	GO-SiO_2	Lightweight, safe	2%	Low shielding performance	This study

Conclusions

The creation and formation of four hybrid nanocomposites have successfully developed physical and functional properties due to their reinforcement with SiO_2 and GO nanoparticles using the casting method. It was shown through structural (XRD, FTIR), morphological (OM, FESEM), and optical (UV-VIS) investigations that the addition of nanomaterials significantly improved the properties, specifically for the NCP3 sample compared to the first sample, which was formed from a blend polymer (PEI-PCL), as it showed the best results in terms of crystallinity, absorbance, refractive index, extinction coefficient, dielectric constants, and gamma-ray attenuation efficiency. This improvement is attributed to the presence of nanomaterials, which in turn leads to better distribution. NCP3 nanocomposite represents a promising material in radiation protection applications, especially for gamma rays and electronics.

Acknowledgements

The authors thank University of Babylon, Iraq, for their support.

Declaration of Generative AI in Scientific Writing

The authors acknowledge the use of generative AI tools (e.g., QuillBot and ChatGPT by OpenAI) only for language editing and grammar correction. AI did not generate content or interpret data. The authors take full

responsibility for the content and conclusions of this work.

CRediT author statement

Sara J. Ahmed: Methodology, Investigated, Analyzed, and Writing – original draft.

Ehssan Al-Bermany: Supervisor, Project administration, Resources, Validation and Editing - final draft.

References

[1] AM El-Khatib, MI Abbas, SI Hammoury, MM Gouda, K Zard and M Elsafi. Effect of PbO-nanoparticles on dimethyl polysiloxane for use in radiation shielding applications. *Scientific Reports* 2022; **12**, 15722.

[2] N Rabiei, L Gholamzadeh, MK Aminian and H Sharghi. Flexible and lead-free polymer composites for X-ray shielding: Comparison of polyvinyl chloride matrix filled with nanoparticles of tungsten oxides. *Radiation and Environmental Biophysics* 2025; **64**, 151-161.

[3] AI Alawi, E Al-Bermany, RS Alnayli, MM Sabri, NM Ahmed and AKJ Albermany. Impact of SiO_2-GO hybrid nanomaterials on opto-electronic behavior for novel glass quinary (PAAm-PVP-PVA/SiO2-GO) hybrid nanocomposite for antibacterial activity and shielding applications. *Optical and Quantum Electronics* 2024; **56(3)**, 429.

[4] SS Türkaslan, SS Ugar, EE Türkaslan and N Fantuzzi. Evaluating the X-ray-shielding performance of graphene-oxide-coated nanocomposite fabric. *Materials* 2022; **15**, 2025

[5] ZJ Kadhim, AA Shaher, K Abdali, NA Al-Ali, E Al-Bermany and AN Tuama. Insights into the microstructure, optical, dielectric, and biological features of HA@MoS reinforced PEO/SA nanocomposite films for optoelectronics, sunscreens, energy storage, and bactericidal applications. *Journal of Inorganic and Organometallic Polymers and Materials* 2025. https://doi.org/10.1007/s10904-025-03805-5.

[6] K Shahzad, A Kausar, S Manzoor, SA Rakha, A Uzair, M Sajid, A Arif, AF Khan, A Diallo and I Ahmad. Views on radiation shielding efficiency of polymeric composites/nanocomposites and multi-layered materials: Current state and advancements. *Radiation* 2022; **3**, 1-20.

[7] A Richert, E Olewnik-Kruszkowska, R Malinowski, A Kalwasińska and MS Brzezinska. Polycaprolactone-based films incorporated with birch tar—thermal, physicochemical, antibacterial, and biodegradable properties. *Foods* 2023; **12(23)**, 4244.

[8] J Casper, SH Schenk, E Parhizkar, P Detampel, A Dehshahri and J Huwyler. Polyethylenimine (PEI) in gene therapy: Current status and clinical applications. *Journal of Controlled Release* 2023; **362**, 667-691.

[9] K Filak-Mędoń, KW Fornalski, M Bonczyk, A Jakubowska, K Kempny, K Wołoszczuk, K Filipczak, K Żerańska and M Zdrojek. Graphene-based nanocomposites as gamma-and X-ray radiation shield. *Scientific Reports* 2024; **14**, 18998.

[10] WM Al-Saleh, HM Almutairi, MI Sayyed and M Elsafi. Multilayer radiation shielding system with advanced composites containing heavy metal oxide nanoparticles: A free-lead solution. *Scientific Reports* 2023; **13**, 18429.

[11] C Kaew-on, J Yuennan, N Tohluebaji, P Channuie, S Ruangdit, R Samran, T Tochomphoo and R Siri. Enhanced hydrophobicity, thermal stability, and X-ray shielding efficiency of $BaSO_4$/P(VDF-HFP) nanocomposites for advanced lead-free radiation protection. *Polymers* 2025; **17(6)**, 723.

[12] MV Paula, LAD Azevedo, IDDL Silva, GM Vinhas and SA Junior. Effects of gamma radiation on nanocomposite films of polycaprolactone with modified MCM-48. *Polimeros* 2021; **31(3)**, e2021031.

[13] MA Kadhim and E Al-Bermany. New fabricated PMMA-PVA/graphene oxide nanocomposites: Structure, optical properties and application. *Journal of Composite Materials* 2021; **55(20)**, 2793-2806.

[14] AN Obaid and E Al-Bermany. Impact of graphene nanosheets on adhesion and corrosion performance of reinforced polyurethane coating for aerospace aluminium alloy 2024-T3. *International Journal of Adhesion and Adhesives* 2024; **132**, 103695.

[15] RA Abdul-Nabi and E Al-Bermany. Performers of Si_3N_4 concentrations on morphology and electrical behavior for new quinary fabrication PEO-CMC-PANI/GO@Si_3N_4 nanocomposites for electronic devise and gas sensor application. *Silicon* 2024; **16**, 5583-5601.

[16] NT Sheehab, FS Hashim, E Al-Bermany, AN Obaid, K Abdali and AHO Alkhayatt. Performance of TiO_2-SiC nanomaterials on morphology and sorption behavior of PVA-PEG-based nanocomposites for UV-applications and antibacterial efficacy. *Nano-Structures and Nano-Objects* 2025; **42**, 101479.

[17] FS Hashim, SA Jabbar, E Al-Bermany and K Abdali. Effect of inclusion ZnO-Co_3O_4 nanoparticles on the microstructural and optical properties of PVA-CMC polymeric blend for biomedical, UV shielding, and nuclear radiation shielding applications. *Plasmonics* 2024; **20**, 1629-1641.

[18] AN Tuama, E Al-Bermany, RS Alnayli, KH Abass, K Abdali and MH Jameel. A critical review of the evaluation of Sio_2-incorporated Tio_2 nanocomposite for photocatalytic activity. *Silicon* 2024; **16**, 2323-2340.

[19] K Abdali. Structural, morphological, and Gamma Ray Shielding (GRS) characterization of HVCMC/PVP/PEG polymer blend encapsulated with silicon dioxide nanoparticles. *Silicon* 2022; **14**, 9111-9116.

[20] E Al-Bermany and B Chen. Effect of the functional groups of polymers on their adsorption behavior on graphene oxide nanosheets. *Macromolecular Chemistry and Physics* 2023; **224**, 2300101.

[21] S Pandey, A Pandey, M Deshmukh and AK Shrivastava. Role of geiger muller counter in modern physics. *Journal of Pure Applied and Industrial Physics* 2017; **7(5)**, 192-196.

[22] A Poškus. *Experiment No. 9: Absorption of alpha particles and electrons*. Vilnius University, Vilnius, Lithuania, 2015.

[23] W Tlaczala and M Zaremba. Virtual experiments in nuclear physics. *In*: Proceedings of the 2007 IEEE Instrumentation and Measurement Technology Conference IMTC, Warsaw, Poland. 2007, p. 1-6.

[24] M Erdem, O baykara, M Doğru and F Kuluöztürk. A novel shielding material prepared from solid waste containing lead for gamma ray. *Radiation Physics and Chemistry* 2010; **79(9)**, 917-922.

[25] D Winkler. 2018, Characterization of a HPGe coaxial well detector for low energy gamma spectroscopy & sensitivity analysis of germanium spectrometers. Bachelor Thesis. Ruprecht-Karls-Universität Heidelberg, Heidelberg, Germany.

[26] R Xu, C Su, L Cui, K Zhang and J Li. Preparing sodium alginate/polyethyleneimine spheres for potential application of killing tumor cells by reducing the concentration of copper ions in the lesions of colon cancer. *Materials* 2019; **12(9)**, 1570.

[27] KPS Hussan, S Inoue, Y Arai, K Sasaki, R Kita, T Ito and N Shinyashiki. Molecular insights into an electrolytic polymer, polyethylene imine. *Polymer* 2025; **321**, 128101.

[28] R Ellerbrock, M Stein and J Schaller. Comparing amorphous silica, short-range-ordered silicates and silicic acid species by FTIR. *Scientific Reports* 2022; **12**, 11708.

[29] E Al-Bermany, AT Mekhalif, HA Banimuslem, K Abdali and MM Sabri. Effect of green synthesis bimetallic Ag@SiO_2 core-shell nanoparticles on absorption behavior and electrical properties of PVA-PEO nanocomposites for optoelectronic applications. *Silicon* 2023; **15**, 4095-4107.

[30] MA Ramazanov, HA Shirinova, SG Nuriyeva, MA Jafarov and MR Hasanova. Structure and optic properties of the nanocomposites based on polypropylene and amorphous silica nanoparticles. *Journal of Thermoplastic Composite Materials* 2023; **36**, 1762-1774.

[31] AA Vassiliou, D Bikiaris, KE Mabrouk and M Kontopoulou. Effect of evolved interactions in poly (butylene succinate)/fumed silica biodegradable in situ prepared nanocomposites on molecular weight, material properties, and biodegradability. *Journal of Applied Polymer Science* 2011; **119**, 2010-2024.

[32] M Fadaie and E Mirzaei. Nanofibrillated chitosan/polycaprolactone bionanocomposite scaffold with improved tensile strength and cellular behavior. *Nanomedicine Journal* 2018; **5(2)**, 77-89.

[33] M Qiu, Y Zhang and B Wen. Facile synthesis of polyaniline nanostructures with effective electromagnetic interference shielding performance. *Journal of Materials Science: Materials in Electronics* 2018; **29**, 10437-10444.

[34] ZJ Kadhim, E Al-Bermany, AA Shaher, NA Al-Ali, K Abdali and AN Tuama. Probing the physical and antibacterial features of SiO_2@MoS_2 nanoparticle-embellished PEO/sodium alginate/PVA matrix for sunscreens, energy storage, food preservation, and unique plasmonic applications. *Plasmonics* 2025. https://doi.org/10.1007/s11468-025-03055-8.

[35] AI Alawi and E Al-Bermany. Exploring the impact of silicon nanoparticles on polymer nanocomposites: Advancements in fabrication techniques and exciting applications in solar cells, photoelectronic, and sensors. *In*: Proceedings of the 2nd International Conference on Scientific Research and Innovation 2023, Ohio, USA. 2023, p. 60007.

[36] SS Aljelawy, E Al-Bermany and AR Abdulridha. Opto-electrical dielectrics and conductivity behavior of vinyl polymers reinforced with chitosan@graphene oxide nanomaterials for optoelectronic and biological activity. *The European Physical Journal Plus* 2025; **140**, 94.

[37] SS Aljelawy, E Al-Bermany and AR Abdulridha. Performance of graphene-functionalized nano chitosan in ternary polymeric nanocomposites for physical and biological applications. *Journal of Polymer Research* 2024; **31**, 226.

[38] J Liggat. Physical chemistry of macromolecules: Basic principles and issues: By S.F. Sun. pp. 469. Wiley, Chichester, 1994. £54.00. ISBN 0 471 59788 0. *Endeavour* 1995; **19**, 132-133.

[39] NR Aldulaimi and E Al-Bermany. New fabricated UHMWPEO-PVA hybrid nanocomposites reinforced by GO nanosheets: Structure and DC electrical behaviour. *In*: Proceedings of the 3rd International Scientific Conference of Engineering Sciences and Advances Technologies, Babylon, Iraq. 2021, p. 12164.

[40] S Deng, J Zhang, L Ye and J Wu. Toughening epoxies with halloysite nanotubes. *Polymer* 2008; **49**, 5119-5127.

[41] RA Abdul-Nabi and E Al-Bermany. Antibacterial and anticancer potentials of graphene-silicon nitride nanomaterials-enhanced polymer nanocomposites: Advanced characterization and optical behavior insights. *Journal of Biosafety and Biosecurity* 2025; **7**, 55-68.

[42] AAF Abodood, K Abdali, AOM Al-Ogaili, E Al-Bermany and KH Abass. Effect of molar concentration and solvent type on linear and NLO properties of Aurintricarboxylic (ATA) organic dye for image sensor and optical limiter applications. *International Journal of Nanoscience* 2023; **22(2)**, 2350014.

[43] VNN Suryawanshi. Band gap engineering in PbO nanostructured thin films by Mn doping. *Thin Solid Films* 2018; **645**, 87-92.

[44] A Kirschning, W Solodenko and K Mennecke. Combining Enabling Techniques in Organic Synthesis: Continuous Flow Processes with Heterogenized Catalysts. *Chemistry - A European Journal* 2006; **12(23)**, 5972-5990.

[45] NA Azahari, N Othman and H Ismail. Biodegradation studies of polyvinyl alcohol/corn starch blend films in solid and solution media. *Journal of Physical Science* 2011; **22(2)**, 15-31.

[46] J Tauc, A Menth and DL Wood. Optical and magnetic investigations of the localized states in semiconducting glasses. *Physical Review Letters* 1970; **25**, 749-752.

[47] M Fox. *Optical Properties of Solids*. Oxford University Press, Oxford, 2010.

[48] S Khammahong, C Phrompet, C Ruttanapun and C Sriwong. Effect of rGO nanosheet loading in SiO_2/rGO hybrid nanocomposites for enhancing optoelectrical, physical, and electrochemical properties. *Diamond and Related Materials* 2025; **155**, 112330.

[49] IR Ghanim, NR Aldulaimi, SA Jabbar, FS Hashim, K Abdali, E Al-Bermany and AN Tuama. Effect of embedding WO_3NPs on the structural, morphological, optical, and dielectric properties of PVA-CMC-PEG polymeric matrix towards optoelectronic and energy storage applications. *Journal of Inorganic and Organometallic Polymers and Materials* 2025; **35**, 1143-1151.

[50] RM Ahmed and E Al-Bermany. Tuning the optical absorption and band gab of hydrogel methylcellulose loaded using hybrid Fe_3O_4@GO

nanomaterials for optoelectronic and antibacterial activity. *Journal of Optics* 2024; **35**, 1143-1151.

[51] A Badawi and SS Alharthi. Developing the optical and radiation shielding of PVA/PVP blend by doping with Fe/NiO nanoparticles. *Journal of the Indian Chemical Society* 2025; **102**, 101752.

[52] MA El-Morsy, NS Awwad, HA Ibrahium and MO Farea. Optical, and electrical conductivity properties of ZnO and TiO2 nanoparticles scattered in PEO-PVA for electrical devices. *Results in Physics* 2023; **50**, 106592.

[53] SJ Ahmed and E Al-Bermany. Performance SiO_2, GO, and SiO_2@GO nanomaterials on fabricating new polymer nanocomposites for optical, antibacterial, and anticancer applications. *Applied Nanoscience* 2025; **15**, 3.

[54] G Soni, N Bhargawa and J Kaur. Fabrication of PMMA/SiO_2 nanocomposite thin films: Optical and microwave radiation shielding properties. *International Journal of Modern Physics B* 2024; **39(16)**, 2550131.

[55] AJ Farhan, K Abdali, E Al-Bermany, RG Kadhim, AN Tuama and AA Thamer. Appraisal of the impact of wrapping Sm_2O_3-SiO_2 versatile nanoparticles on the structural, morphological, optical, and dielectric properties of PEO|SALG polymeric blend for optoelectronics, UV absorbance, and energy storage attributes. *Journal of Inorganic and Organometallic Polymers and Materials* 2025; **35**, 3169-3181.

[56] G Soni, N Gouttam and V Joshi. Synthesis and comparisons of optical and gamma radiation shielding properties for ZnO and SiO_2 nanoparticles in PMMA nanocomposites thin films. *Optik* 2022; **259**, 168884.

[57] S Mansouri. Multi-nanoparticle-based composite for diagnostic X-ray shielding in computed tomography applications: A Monte Carlo study. *Radiation and Environmental Biophysics* 2025; **64(2)**, 263-274.

[58] ME Mahmoud, AM El-Khatib, AM Halbas and RM El-Sharkawy. Ceramic tiles doped with lead oxide nanoparticles: Their fabrication, physical, mechanical characteristics and γ-ray shielding performance. *Radiation Physics and Chemistry* 2021; **189**, 109780.

[59] MS Rise, AH Ranjbar, H Noori and V Saheb. Bi-PMMA composite materials and their shielding capability for low energy gamma rays. *Radiation Physics and Chemistry* 2023; **212**, 111201.

[60] D Cao, G Yang, M Bourham and D Moneghan. Gamma radiation shielding properties of poly (methyl methacrylate)/Bi_2O_3 composites. *Nuclear Engineering and Technology* 2020; **52**, 2613-2619.